UNIVERSITY OF TWENTE

BMT MODULE 12: BACHELOR THESIS
RESEARCH GROUP: MULTI-MODALITY
MEDICAL IMAGING (M3I)

Design and testing of a breast perfusion tumor phantom for dynamic contrast-enhanced Computed Tomography

Sanne Gouma (s2501481)

Committee:
Chair: Sechopoulos, Ioannis, prof.dr.
Daily supervisor: Goris, Liselot
External member: dr.ir. David Thompson
Additional external member: Pautasso, Juan

03-07-2024

Abstract

Breast cancer is the most prevalent cancer among women, accounting for 25% of all cancer diagnoses worldwide. Early and reliable detection and monitoring techniques are essential for effective treatment. This study focuses on Dynamic Contrast-Enhanced dedicated Breast Computed Tomography (DCE-bCT). The aim is to develop a tumor phantom combined with an existing breast phantom and an optical spectrometer setup to evaluate DCE-bCT as a potential monitoring technique for breast cancer.

3D printing methods, including fused deposition modelling (FDM) and stereolithography (SLA), were used to fabricate the phantoms. The tumor phantom was designed to mimic the complex vascular structures of tumors, incorporating small gyroid structures (pores sizes of 1.3 and 1.5 mm), internal channels (0.8 - 1 mm diameter) and leaking vessels. To ensure air-free phantoms, the proper filling technique and running fluid composition (49.5% water, 49.5% glycerol and 1% Ilfotol), were investigated, and results were evaluated with cone beam CT.

Three final phantom designs were tested using DCE-bCT after they fulfilled all the requirements. Each of the final phantoms featured at least two distinct regions that created different flow patterns, designated as regions of interest (ROIs). For each ROI, a time-intensity curve (TIC) was planned to be generated, allowing intraphantom comparisons to assess the distinguishability of ROIs using DCE-bCT. The phantoms designed in this study were compatible with the setup. Flow was successfully passed through the phantom without air being trapped inside. The optical spectrometer data showed the expected wash-in and wash-out pattern created. Due to uncontrollable circumstances, no time-intensity curves have been created for the different tumor phantom designs. The results of the tumor phantom research and the DCE-bCT breast cancer monitoring method can be verified by interpreting the curves later on.

Contents

1   Introduction

The World Health Organization (WHO) gives the following definition of breast cancer: "Breast cancer is a disease in which abnormal breast cells grow out of control and form tumors. If left unchecked, the tumors can spread throughout the body and become fatal" [1]. 19.3 million cancer cases worldwide were detected in 2020 [2]. 2.3 Million of these cases were breast cancer diagnoses in women, representing 25% of all cancer diagnoses for women, making it the most prevalent cancer for them. The American Cancer Society has reported an average annual increase of 0.3% in breast cancer diagnoses since 2004 [3]. From 1989 to 2017, the mortality rate dropped 40%, reflecting the effect and importance of early and reliable detection techniques.

1.1   Detection and diagnosis

With the high occurrence rate of breast cancer, reliable and widely available screening methods are essential. The most common detection techniques are briefly explained below.

Self-examination is the most accessible and basic technique to test for breast cancer; the patients feel with their fingers for abnormal swelling or lumps in the breast. Mammography is a clinical diagnostic technique that uses X-rays to image the breast. The procedure starts with compressing the breast and then sending an X-ray burst through it. A detector captures the X-rays that pass through, creating an image based on the different attenuation coefficients for the varying tissues. This process is repeated in a second plane for enhanced detection [4]. Radiologists then assess for the presence of cancer and the need for further tests. Dutch women aged 50-75 are invited for government-funded biennial mammography screenings, targeting the demographic with the highest risk [5, 6]. In 2022, 2.4% of screened participants were referred for additional evaluation [7]. Drawbacks include radiation exposure, false positives, and over-diagnosis [8]. Dense breast tissue can also obscure tumor detection [9].

Tomosynthesis or 3D mammography is a diagnostic technique similar to mammography; it uses X-rays for detection. The difference is that the X-ray machine moves in a fifty-degree arc around the breast; these images are used to construct a 3D breast model [10]. This technique reduces false positive diagnoses but increases the effective dose by 22% [11, 12, 13]. Synthesised mammography images can be formed from a tomosynthesis scan and are valuable when they reveal tumors missed by standard mammography [14]. Ultrasound can be used alongside mammography for women at higher risk for breast cancer. This technique uses high-frequency sound waves to image the breast. Adding ultrasound to a mammogram improves detection rates, especially in women with dense breast tissue, but may result in more follow-up calls [15]. Ultrasound does not carry health risks and is also used as a guidance tool for taking biopsies. Further, this technique can also distinguish between a cyst or a solid mass inside the breast [16].

1.2   Monitoring techniques

Magnetic resonance imaging (MRI), when added to mammography and ultrasound for high-risk women, significantly boosts detection rates [17]. The advantage in detection lies in a lower interim cancer detection rate between two mammography screening rounds because smaller tumors can be detected with MRI, which mammography alone would have missed [15]. This technique can also be used for treatment monitoring, showing changes in tumor size, vascular density, and homogeneity [18]. To better investigate changes, contrast can be added; the most used is gadolinium. Contrast agents enhance detection due to the high vascularity and permeability of the tumor vessels [19, 20]. Dynamic contrast-enhanced MRI (DCE-MRI) has shown promising results in monitoring tumor changes and in specificity of the diagnosis [21, 22]. Metabolic and vascular changes after chemotherapy have been displayed on DCE-MRI after one round of treatment before shrinkage could be noticed [23]. Breast Computer Tomography is a monitoring technique that uses X-rays for imaging. A 360-degree scan of the breast is made without compression, offering patient more comfort and a full 3D image of the breast compared to mammography and tomosynthesis. DCE-MRI limitations lay in the temporal resolution and scan time. Dynamic contrast-enhanced breast Computed Tomography (DCE-bCT) addresses these limitations. A digital phantom study to validate DCe-bCT has been developed and showed promising results [24]. A phantom study showed that iodine uptake and concentration can be determined over time with DCE-bCT [25]. Time-intensity curves (TICs) can be formed for regions of interest (ROI), showing different TICs for the tested pumping programs.

With the promising digital DCE-bCT phantom and successful iodine monitoring over time showing promising results for DCE-bCT as monitoring technique [24, 25]. A further phantom study was proposed to validate the DCE-bCT for breast cancer monitoring using the same setup that validated the iodine uptake over time.

1.3   Aim

This research aims to develop a tumor phantom complaint with an existing breast phantom and a setup that measures iodine concentration over time. The purpose is to test distinguishability for the different regions inside the phantom, representing the heterogeneity of tumors, by analysing the corresponding TICs.

2   Theoretical background

The theoretical information that forms the background of this research is presented in this chapter. Offering more detailed information on DCE-bCT and the TICs generated. The fabrication process and some starting choices for the phantom design are also presented in this chapter.

2.1   Dynamic contrast-enhanced breast Computer Tomography

The breast Computed Tomography (bCT) uses X-rays to image the breast. For this technique, the patient lays flat on the table, with one breast positioned inside the dedicated hole, a picture of a bCT is shown in Figure 1. The detector and the X-ray source spin around to make a 360° scan of the breast. These parts named above are inside the white cast. The dynamic part of DCE-bCT involves measuring the wash-in and wash-out of an iodine contrast agent inside the breast. With the different structures inside the breast, each region has a specific TIC. In Figure 2, the difference TICs for tumor and parenchyma are shown as results of a digital phantom study, showing clear difference in wash-in and wash-out for the different structures [24]. To validate the quantitative accuracy of the DCE-bCT a phantom study was preformed. A specific breast phantom has previously been constructed, missing a tumor inside [26]. The purpose of the tumor phantom design is to have distinct region, that mimick tumor heterogeneity with varying vascular densities as closely and to test the DCE-bCT on the phantom [27, 19].

**Figure 1:** Picture of a breast CT [28].
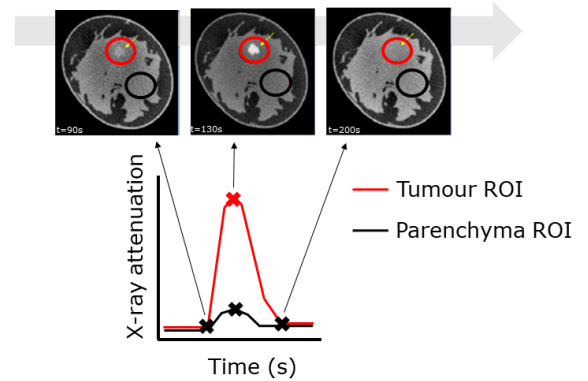
Figure 2: Time intensity curve (TIC), expected data with the measurement. Adaptation of the digital phantom [24].

2.2   Breast tumor

For the form of the tumor, it was chosen to first work with a simple sphere, since the focus was on the inside of the phantom. A diameter of 15 mm was chosen for the sphere, staging it as a T1 tumor. This method of staging is based solely on the size of the tumor [29]. However for real tumors, staging may include more factors, like hormone expression (estrogen and progestogen), HER2 statuses, proliferation index, gene expression-based scores, next to size and metastases, providing a more reliable representation of the disease progression [30].

A tumor has very dense and complicated vascular structures and the tendency to leak into surrounding tissue [19]. To recreate the complicated internal flow structure of a tumor, multiple studies have been done in the past. Prior tumor phantoms used molding techniques or small tubes to recreate the internal structures [31, 32]. For this research 3D printing was used to recreate the internal structures. Based on a liver phantom study, a gyroid structure was proposed to recreate the tumor vascular struture, a picture of a gyroid structure is shown in Figure 4 [33]. An optical spectroscopy setup was used to monitor the iodine wash-in and wash-out over time, a schematic representation of the setup is shown in Figure 3 [25].
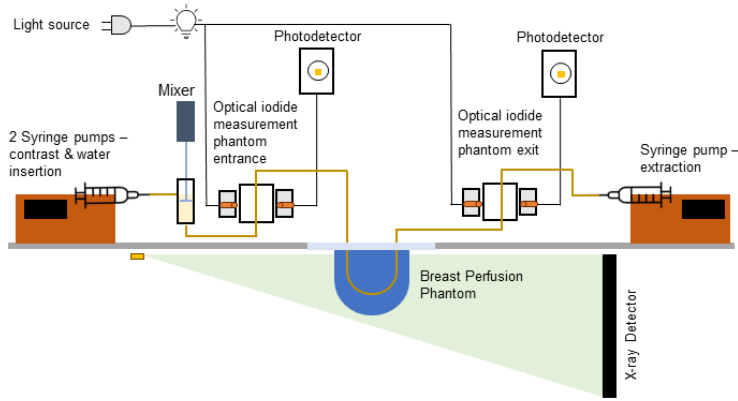
Figure 3: An optical spectroscopy setup [26]. Setup used to create different Iodine concentration profile curves with different pumping programs. Inlet and outlet spectrometer are used as validation method for the TICs created with the DCe-bCT.
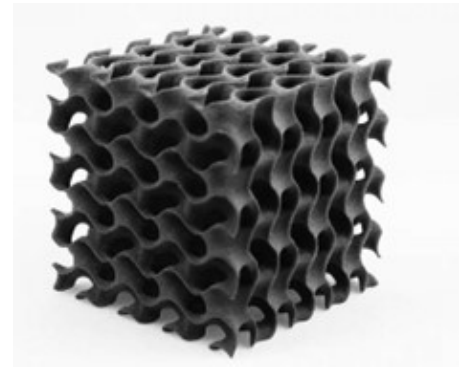

Figure 4: Overview of a gyroid structure [34]. Gyroid structure is used as inside of the phantom, the fine pores recreate the complex internal vascular structure.

2.3 3D printing

The 3D printing techniques used are Fused Deposition Modeling (FDM) and Stereolithography (SLA) printing. Schematic picture of the printers are shown in Figure 5 and 6. FDM uses thermoplastic filaments, this type of material is heated inside the nozzle and printed in layers according to the sketch [35]. The material used for the tumor phantoms is blue Polylactic Acid (PLA).

For SLA printing a laser is used to harden the plastic. The building plate is lowered into a bath filled with clear resin using a screw mechanism. The laser traces the design of that specific layer and hardens it using UV-light. The building plate moves upwards and the uncured material is removed from the building plate with the sweeper, this process is repeated for each individual layer [35]. A schematic picture of SLA printers is shown in Figure 6.
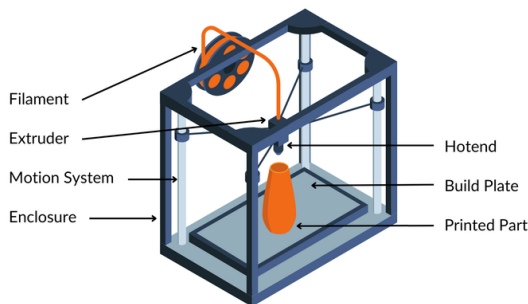
Figure 5: FDM printer [36]. The nozzle melts the filament and the printer then traces the uploaded sketch using the motion system. The layer thickness for the prints is 0.4 mm.
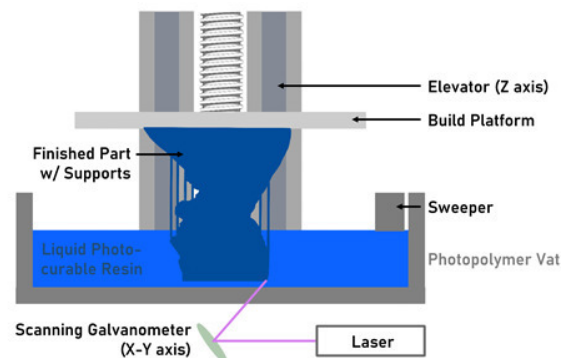
Figure 6: SLA printer [37]. The building plate is lowered into the material. The laser hardens the material according to the sketch, and extra material is removed with the sweeper. The layer thickness of the prints is 0.05 mm.

3   Requirements

With a better understanding of the bCT, breast tumors and 3D printing, a list of requirements is made for the tumor phantom. The requirements can be divided into two groups. The first is the phantom requirements, these represent all materials requirements for the phantom to represent a breast tumor on CT scans. The function requirements make up the second group. These functional specifications have been established in order to make the phantom accurately depict the vascular behavior of a tumor. In Table 1, an overview of the requirements and solutions is presented.

3.1   Overview set requirements

Below is a brief description of the requirements and their relevance. In order to fulfill the specified requirements, the solutions provided in Table 1 for each requirement can be integrated for the final design.

Table 1: Overview of all the requirements and the possible solutions for the tumor phantom.

Phantom requirements	Solution 1	Solution 2	Solution 3	Solution 4
Modular, easy-to-remove	3D printing with connection points for placement in setup	-	-	-
tumor form	Simple sphere	Segmentation of patients tumors form CT scans	Free drawing combined with literature for size and form	-
X-ray attenuation	clear resin for SLA printing	PLA for FDM printing	-	-
Waterproof	SLA printing	FDM printing, outside with high density	Epoxy coating for non-waterproof phantoms	-
Function requirements	**Solution 1**	**Solution 2**	**Solution 3**	**Solution 4**
Air-free	Different sizes of internal structure	Increasing viscosity	Vibrating plate with smoothing solution	Vertical filling
Simulate tumor Blood Flow	Different pattern sizes within a phantom	Two inputs for one phantom, pumping with different velocities	-	-
Anatomical representation of the vascularization of the tumor	Gyroid structure to mimic vascularization	Casting and moulding with small tubes to recreate vessels, remove afterwards	Printing small vessels inside the sphere with 3D printing, ensuring that the channels do not get clogged	First, print the internal structure and then add the outside, ensuring water tightness

• Simulation of tumor blood flow
This research aims to validate DCE-bCT as possible imaging technique to monitor breast tumors. Change in blood flow is an important parameter for treatment responses and tumor progression [?]. Therefore, different flow patterns must be created within the phantom. TICs will be generated for the different areas to test distinguished between the with the help of DCE-bCT.

• Anatomical representation of vascularization
To represent the tumor blood flow, the vascularization inside the tumor must be recreated. Hence, flow must be possible inside the tumor, while recreating the complex internal vascularization inside the tumor. These structures must be big enough, so they do not get clogged with material during 3D printing.

• Modular, easy-to-remove -The phantom that is created, must be able to fit inside the breast phantom. During the testing phase, easy swapping between the phantoms is favorable.

• tumor form
To get the most reliable results for the phantom study, the phantom must be as close to reality as possible. For this study, a simple sphere with diameter of 15 mm was used, to represent a T1 staged breast tumor [29].

• X-ray material
The phantom material must have the same X-ray attenuation properties as tumor tissue. This attenuation is similar to that of fibroglandular tissue. PLA for FDM printing and clear resin for SLA printing have these desired attenuation properties [38].

• Waterproof
For the DCe-bCT the tumor phantom is placed inside a breast phantom. This breast phantom is filled with olive oil. Olive oil recreates the attenuating behaviour of fatty tissue in the breast [39]. To ensure that the olive oil does not mix with the blood-mimicking fluid and contrast mixture used for creating the TICs, the tumor phantom is required to be waterproof.

• Air free
Air is known to give a black signal on CT images and to lower the image quality. Therefore it is important to get the tumor phantom filled air-free. Preventing the air to intervene with the ROI and affect the TICs.

4   Design and Fabrication

This section shows the various designs that led to the final design. The designs were first tested on the Cone Beam CT at TechMed Centre located at the University of Twente. The final designs were used for the measurements on the DCE-bCT system.

To start the designing phase, a gyroid structure was chosen to represent the tumor vascularisation and FDM printing was chosen as fabrication methode. A built-in option for gyroid support was present in the Ultimaker Cura software used for the Ultimaker printer, present at TechMed Centre. The first phantom design proposed, was to print a hollow sphere with connection points and add gyroid support inside the sphere. The support density could be adjusted to obtain the desired pore sizes for the tumor phantom, while still allowing for flow.

4.1   FDM 3D-prints

The first design idea was created in SOLIDWORKS. It consisted of a sphere with an inner circle radius of 6.5 mm and an outer circle radius of 7.5 mm. On both sides, a connection point for a tube was designed. The design for the connection point was a cylinder with an inner radius of 1.1 mm and an outer radius of 2.0 mm. The inner cylinder was hollow, allowing for flow through the phantom. Some structure was added to the connection points to enhance the connection between the phantom and the tubing.
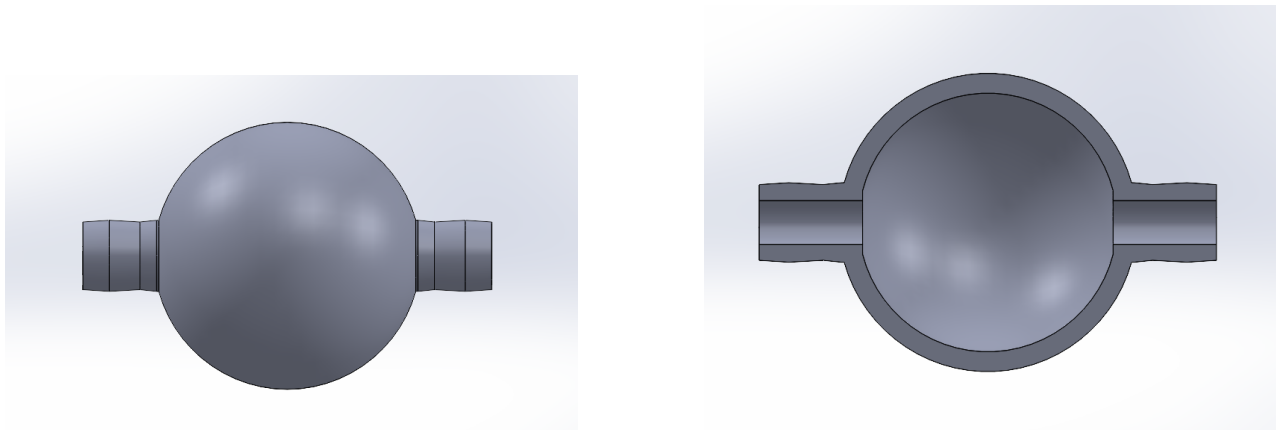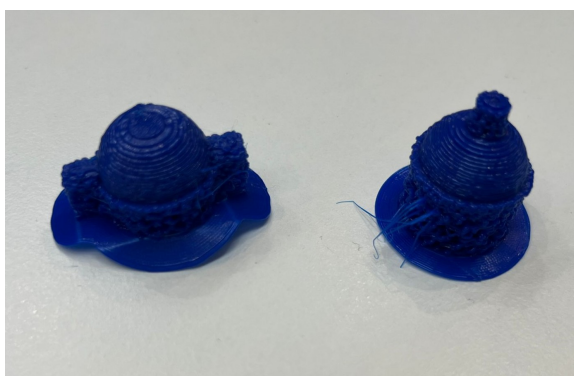

(a) Front view of the phantom. Tubing can be placed around the connection points to allow for flow through the phantom. Structure on outside connection points was added to improve connection with the tubing.

(b) Cross-section of the phantom showing the interior. The sphere has an internal diameter of 13 mm and an outer diameter of 15 mm. Two connection points are created to attach tubes to the setup.

Figure 7: Hollow sphere phantom design used for FDM printing. A gyroid structure is added inside the hollow sphere when support is added for printing. Figure 7a shows a front view, and Figure 7b the cross-section.

The first design was printed using the FDM 3D printing technique and blue PLA filament as material. However, it became clear that FDM printing was not the best option for the phantom. The most significant advantage of filament printing is the relatively low material cost and purchase of this printer compared to SLA printers. However, the detail level is limited since this printer's layer thickness is 0.4 mm. This could also be seen in the first prints since every layer was distinguishable to the eye.

Figure 8 shows the printed FDM phantoms. The prints clearly show that a surplus of support was printed. The phantom design was printed horizontally and vertically to see if that made a difference regarding support removal. The attempts to remove the support entirely on the outside were both unsuccessful. Support was also printed inside the connection points, blocking the possibility of flow through the phantom. There were also concerns that these prints would not be waterproof; however, this could not be tested. It was decided to continue this project with a resin printer because more detailed prints are possible with an SLA printer.

Figure 8: Hollow sphere phantom printed with FDM printer. Support is impossible to remove entirely; no flow is possible due to the phantom's clogged connection points.

4.2   SLA printing

It was decided that SLA printing was a preferred fabrication methode for the new prints. A layer thickness of 0.05 mm could be selected for the phantoms, making a smoother outer layer possible. The chosen clear resin material is also known to be waterproof. The automatically generated support by PreForm has only small connection points to the print, making it easier and possible to remove all the support. The material used was clear resin, which has the additional benefit of being transparent, making it possible to see the inside structure of the phantoms.

After SLA prints are done, a cleaning step has to follow. For clear resin, isopropyl alcohol (IPA) is used as a cleaning solution. First, the prints are removed from the building plate, afterwards all the support is broken from the prints. The prints are placed in an IPA bath for 5 minutes, and each phantom is flushed through with a syringe full of IPA. The printer's building plate is then cleaned with IPA. These cleaning steps are essential to remove all the uncured material on the inside and outside of the phantoms. After the IPA bath, the prints are placed inside a 60°C oven for 15 minutes to harden the prints further with a combination of heat and UV-light.

4.2.1   Gyroid phantom design

For this SLA printer, the design of the hollow phantom had to be altered. Since the gyroid support is not a built-in option in the PreForm software used for the SLA printer. The gyroid structure was recreated in SOLIDWORKS [40]. The sketch created for the gyroid structure cube, is comparable to Figure 4. This file is used to design all the gyroid phantom iterations. A circle with a radius of 6.5 mm was cut from the cube. An outer circle with a radius of 7.5 mm was created around the inner circle, two connection points were secured to the outside for the tubing. The outer diameter of the connection points was 4 mm and the inner diameter was 2.2 mm. The inside of the connection points was hollow, making flow possible through the phantom. For this design, the main uncertainty was how small the gyroid structure could be printed, while still being able to remove all the uncured material on the inside. For the first attempt, a pore size of 1.3 mm was tried. Different views of the gyroid phantom design can be seen in 9.
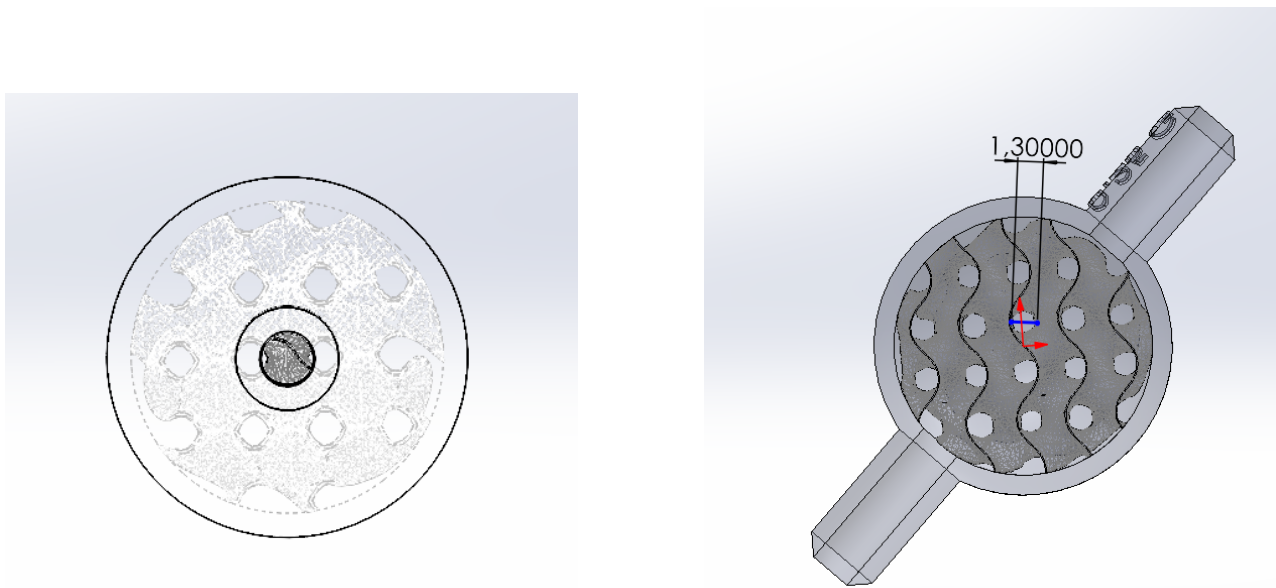
(a) Front view of the phantom. The outer diameter of the connection points is 4 mm and the inner diameter is 2.2 mm. The outer sphere has a radius of 7.5 mm, the inner sphere radius is 6.5 mm.

(b) Phantom cut through the middle, inside visible. The pores have a diameter of 1.3 mm. Outer diameter of the connection points is 4 mm and the inner diameter is 2.2 mm.

Figure 9: Hollow sphere, with internal diameter of 13 mm and outer diameter of 15 mm. Two connection points secured to the outside. The inside for the connection point is hollow, allowing for flow.

4.2.2   Design alterations

Additionally, a more straightforward design was chosen in anticipation that it would help eliminate extra resin and release any trapped air compared to the gyroid phantom. This design consisted of channels through the phantom sphere. The first printed channel phantom had eight channels with a diameter of 2.2 mm on the outside and one channel through the middle with a diameter of 1.1 mm. The second printed channel phantom had eight outer channels and one through the middle, all with a diameter of 1.1 mm. These two channel phantoms designs can be seen in Figure 10.


Figure 10: Channel phantoms, one with eight 1.1 mm diameter channels (left) and one with eight 2.2 mm diameter channels (right). Both have a 1.1 mm diameter channels straight through the middle.
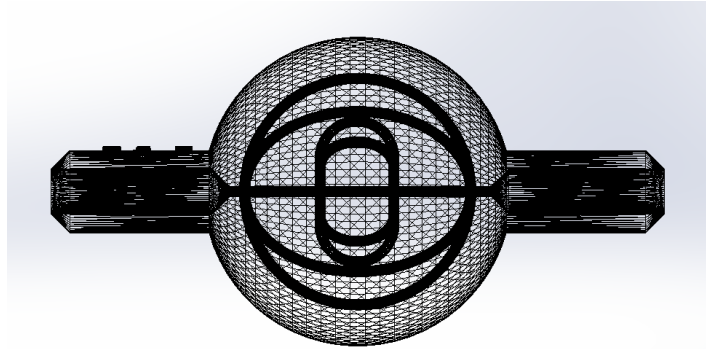
Figure 11: Phantom cut through the middle, showing the inside. The outer diameter of connection points is 4 mm and the inner diameter is 2.2 mm.

Next to the channel phantoms, a double-channel phantom was also created; this design can be seen in Figure 11. The 1.1 mm channel phantom was used as basis for this phantom. Eight smaller channels were added and connected to the channel straight through the middle, creating a more complex flow pattern than the original design. All channels have a diameter of 1.1 mm in this design.
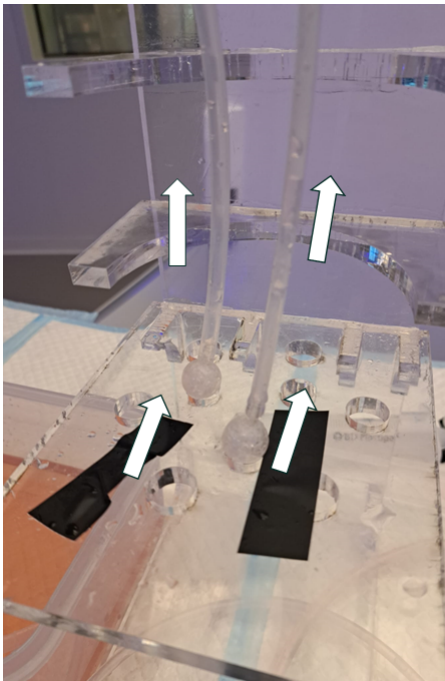
Figure 12: Phantom setup for first CB-CT. For vertical filling, the phantom was filled from below with the mixtures, using a syringe pump. Tubing on top led to a residue container. Flow direction indicated with arrows.

These first SLA-printed phantoms were tested with the ConeBeam CT available at TechMed Center. For the first measurement session, a mixture of water and food colouring, as well as blood-mimicking fluid, were used. The blood-mimicking fluid consisted of 50% water, 50% glycerol, and a few food colouring drops [41]. The latest ingredient is added to the basis of blood-mimicking fluid to enhance visibility of air with the eye in the mixtures. Both mixtures were thoroughly mixed before filling a 60 ml syringe with each. The phantom was placed in a holder, as shown in Figure 12. One syringe at a time was placed in a syringe pump; the pump was connected to the phantom inlet using tubing. The tubing used throughout the research has inner diameter of 3 mm and is flexible. The outlet of the phantom was connected to a waste reservoir again with tubing. The pump was started, and a CT scan was performed while the phantom was flushed with one of the mixtures. Horizontal and vertical flushing of the phantom were additionally tested during this session. The CT scans presented in Table 2, include a selected part of the initial CB-CT results.

It was chosen to continue with blood-mimicking fluid, since it represents blood viscosity and positively affects air removal compared to the water and food colouring mixture. Vertically filling of the phantom was also chosen, since it resulted in less air trapped inside the phantom. The inlet side was at the bottom, forcing the air out of the phantom with the flow and gravity. The holder and vertically placed phantom can be seen in Figure 12. The CT scans with vertical filling and the blood-mimicking fluid are presented in Table 2 for these phantoms.

Table 2: Overview of the acquired CT scans. The scans inside the table, are all made with blood-mimicking fluid and vertically filling.


LT: slice 283/467 from the CT from 1.1 mm channel phantom. Air is visible and marked with the arrows.

RT: slice 183/467 from the CT from 1.1 mm double channel phantom. Air is visible and marked with arrows. More are was trapped that in 1.1 channel phantom when full scan was analysed.

LB: slice 198/467 from the gyroid phantom. Air is visible and marked with arrows. Gyroid structure was bigger than on the right, less air was therefore trapped.

RB: slice 128 from the gyroid phantom. Air is visible and marked with arrows. Most air was trapped in this phantom compared to the other phantoms in the table.

4.3   New designs and protocol

The first CB-CT scans showed in Table 2, that air remained trapped inside all the phantom designs. Therefore, the designs and cleaning process were adjusted. The measurement protocol was also investigated, all with the goal of preventing air from entering the phantoms. It was decided not to continue with the double-channel phantom since most air stayed trapped inside this design and to focus on adjustments for the channel phantom and the gyroid phantom.

4.3.1   Channel phantom

The channel diameter was altered for the channel phantom to test how small they could get before getting clogged with material while printing. The channel straight through the middle was also dropped. This way, the flow pattern would be the same through all eight channels. This was thought to help the air get out of each channel since there is no preferable route for the flow. The inner diameter of the connection points stayed at 2.2 mm. The outer diameter was changed to 4.3 mm; the length of the connection points was changed from 7 to 9 mm. Both changes were made to enhance the connection between the tubing and the phantom's connection points and prevent leakage, , experienced during the first session. The altered design was printed for 0.8 mm and 0.5 mm diameter channels. After the print was finished, it became clear that a diameter of 0.5 mm was too small for the channels, as the channels in this design were clogged. However, the design with a 0.8 mm channel diameter was suitable for CB-CT testing. This design can be seen in Figure 13.
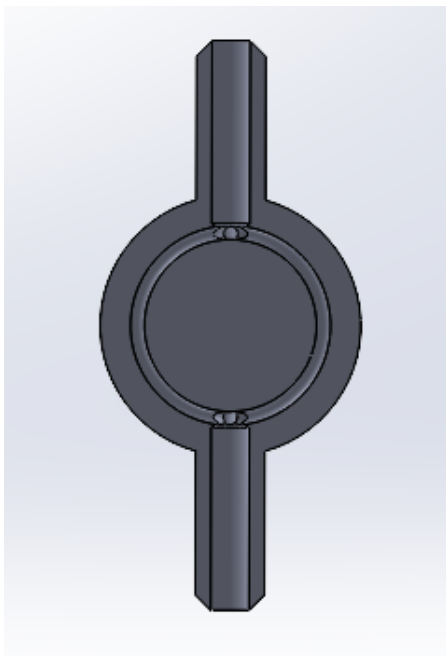

(a) Cross section of channel phantom with 0.8 mm channel diameter. Eight channels are created inside the sphere. The connection points are 9 mm long, have inner diameter of 2.2 mm and outer diameter of 4.3 mm. The channels and connection points are hollow, allowing flow through the phantom.
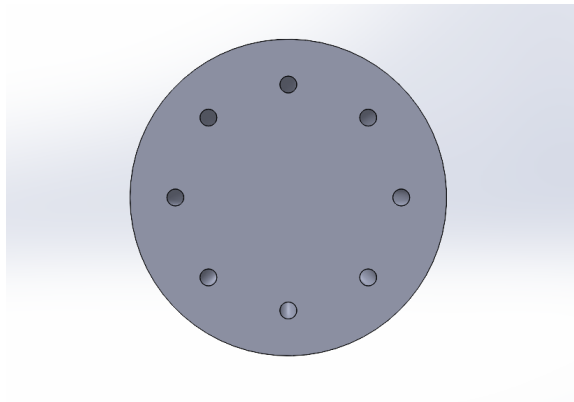
(b) Sphere of the phantom cut through the middle. Eight evenly spaced channels with 0.8 mm diameter are visible.

Figure 13: Channel phantom, images showing different perspectives of the eight 0.8 mm diameter channels inside the phantom.

For the gyroid structure, the sphere radius was increased from 7.5 mm to 9 mm. The design had still a solid outer sphere with a thickness of 1 mm. The gyroid pore size was increased from 1.3 to 1.5 mm. These adjustments were made to enhance the cleaning process, promoting air removal out of the phantom. The same cube gyroid structure was used, but this time, a scaling factor was used to create a bigger pore size before cutting out the gyroid sphere. For this design the same size for the connection points were used as for the 0.8 mm channel phantom. Different views of this design can be seen in Figure 14.
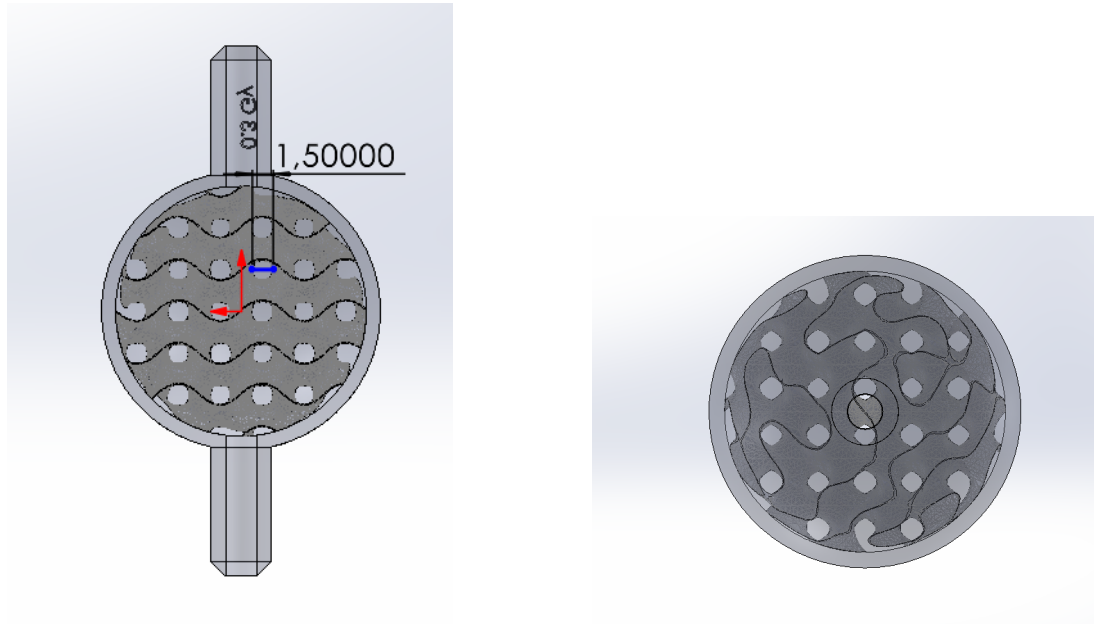
(a) Gyroid phantom, connection points have a length of 9 mm. Inner diameter of the connection points is 2.2 mm and the outer diameter is 4.3 mm. The radius of the sphere is 9 mm. The pore size for this design is 1.5 mm, and indicated explicit in the figure.

(b) Front view of the gyroid phantom design. One connection point is shown from the top.

**Figure 14:** Gyroid phantom images showing different perspectives.

4.3.2   Cleaning alterations

After the phantom prints were finished, the cleaning steps took place. For the first designed prints, this meant placing them in a bath full of IPA for 5 minutes and being flushed through with a syringe filled with IPA. After this, the prints were placed in an oven at 60°C for 15 minutes, curing them further with heat and UV-light. After the second design round and the first CB-CT results, the cleaning process was extended. The IPA in the bath was changed for the second round, ensuring that the bath was not saturated with the excess clear resin from previous prints. Blowing compressed air through the phantoms was also added as an additional step; this was done to remove all the uncured resin before placing the phantoms in the oven. The new cleaning protocol also included two rounds of flushing IPA through the phantom alternated with compressed air. This was done to remove the extra resin in the phantoms. The oven step remained untouched, after the cleaning was done.

4.3.3   Protocol adjustment

For the second CB-CT measurement, not only did the designs and cleaning process change, but the measurement setup and protocol were also investigated. Since the first CT session showed air inside all the phantom, the focus was on getting the phantom air free. The solutions for removing air from the phantoms shown in Table 1 were combined, leading to a new measurement procedure. The basis for the for the blood-mimicking fluid stayed the same. Additionally, 10 ml of Ilford Ilfotol was added to 1 litre of the glycerol-water mixture as a smoothing solution. The smoothing solution reduces the static forces on the air bubbles created by the adhesion to the internal structures of the phantoms.

The setup was altered by adding a vibrating plate, a new phantom holder, and a different type of pump. The new phantom holder is shown in Figure 15 and the full overview of the setup is shown in Figure 16. The reservoir was filled with the new mixture and connected to the pump. The pump was connected with tubing to the phantom's inlet, located downwards in the phantom holder. The phantom's outlet was connected from the top back to the reservoir with tubing. The pump was started, and filled the phantom, while the vibrating plate was turned on. From time to time, it was checked if air bubbles were visible inside the phantom; when this was the case, the vibrating plate was turned back on. Trying again to remove the air inside. The flow direction was also altered using the pump, when air bubbles seemed stuck inside the phantom. When no air bubbles were visible to the eye, a CT scan was made to confirm. If the CT scan showed air was present inside the phantom, a new attempt was made to remove the air. The CT scans for the new channel and gyroid phantom designs are presented in a table on the next page. Both phantoms were filled successfully without air trapped inside the phantom.
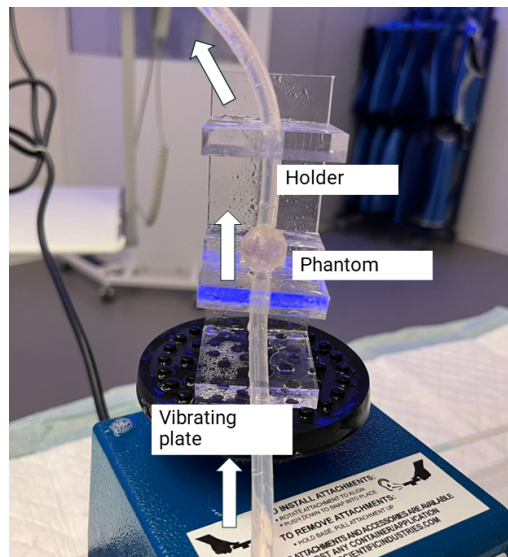
Figure 15: Phantom holder, with a gyroid phantom placed in the setup. The holder is placed on a vibrating plate.
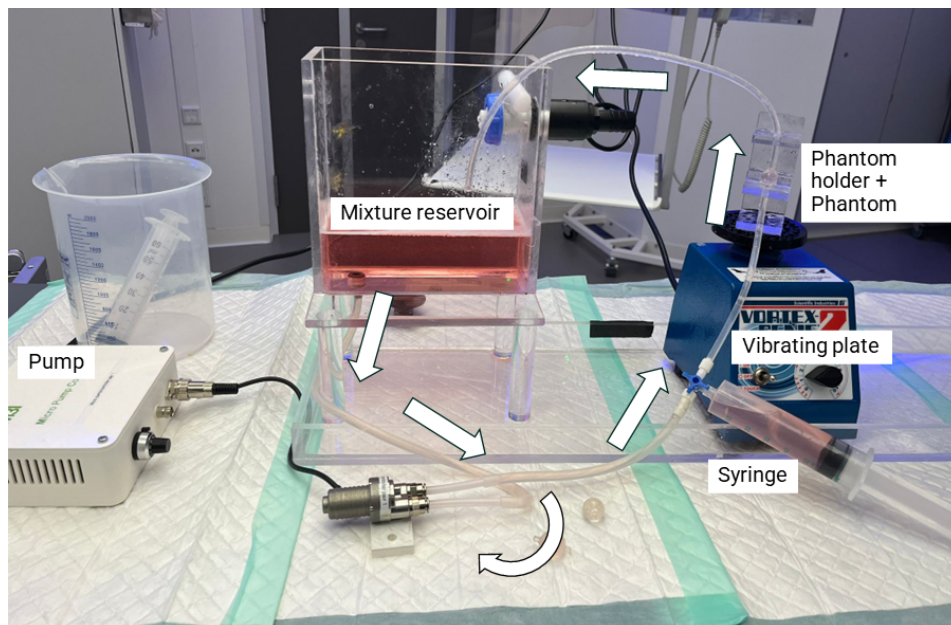
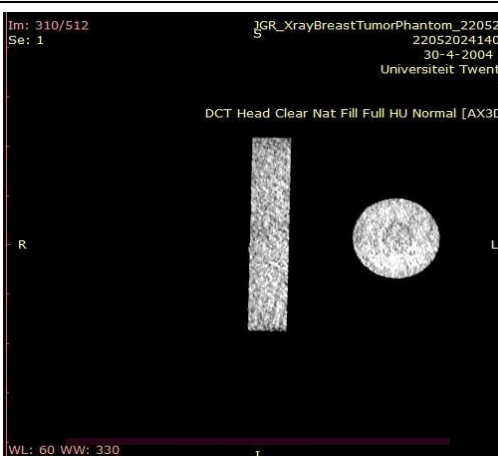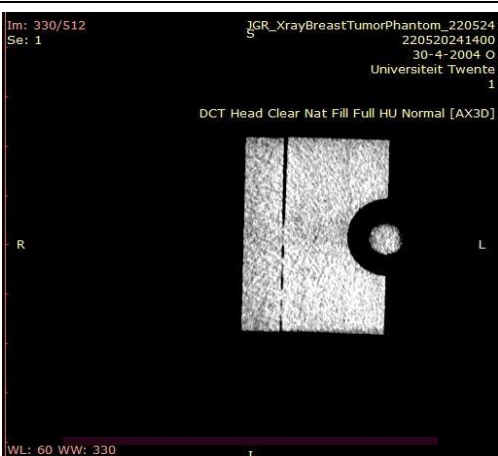**Figure 16:** On the left, the new pump can be seen. The tubing leads the mixture from the pump to the phantom, placed inside the holder on the vibrating plate. The outlet is connected to the reservoir with the mixture, which recirculates in the setup.

Table 3: CB-CT overview for 0.8 mm channel phantom. Table showes that no air is present inside the phantom.

CB-CT slices second session 0.8 mm channels	
LT: slice 228/512 from the CT from 0.8 mm channel phantom. No air is visible. The scan is from bottom to top for the phantom inside the holder.	RT: slice 248/512 from the CT from 0.8 mm channel phantom. No air is visible. The scan is from bottom to top for the phantom inside the holder.
LB: slice 268/512 from the CT from 0.8 mm channel phantom. No air is visible. The scan is from bottom to top for the phantom inside the holder.	RB: slice 288/512 from the CT from 0.8 mm channel phantom. No air is visible. The scan is from bottom to top for the phantom inside the holder.

Table 4: CB-CT overview for gyroid phantom with pore size of 1.5 mm. Table showed that no air is present inside the phantom.

CB-CT slices second session gyroid phantom

LT: Slice 230/512. No air visible inside the gyroid phantom

RT: Slice 250/512. No air visible inside the gyroid phantom

LM: Slice 270/512. No air visible inside the gyroid phantom

RM: Slice 290/512. No air visible inside the gyroid phantom

LB: Slice 310/512. No air visible inside the gyroid phantom

RB: Slice 230/512. No air visible inside the gyroid phantom

5   Final designs

The 0.8 mm channel phantom and the new gyroid phantom were successfully filled without air in the second measurement session with the CB-CT, as shown respectively in Table 3 and Table 4. These designs formed the basis for the final designs. An overview of all the designs made is presented in Appendix B. In Appendix A, a design for a leaking gyroid phantom is presented, however this design is not further investigated. One requirement not met with prior designs for the breast tumor phantom was to generate distinct contrast curves within the phantom. To achieve this, the latest designs were modified to include diverse regions, thereby introducing varying flow patterns within the phantom. Testing the distinguishability between these regions was facilitated using the created Time Intensity Curves (TIC).

A theoretical TIC was also presented in the literature for the pumping program used for the dynamic measurements, presented in Figure 17. Presenting the results that validated the DCE-bCT and formed the basis of this research [26]. Instead of just the tube, the breast phantom will contain an additional tumor phantom, for further testing of the DCE-bCT.

(a) ROI for the theoretical contrast curve, using DCE-bCT to generate a TIC.

(b) TIC based on the pumping program and ROI shown in Figure 17a.
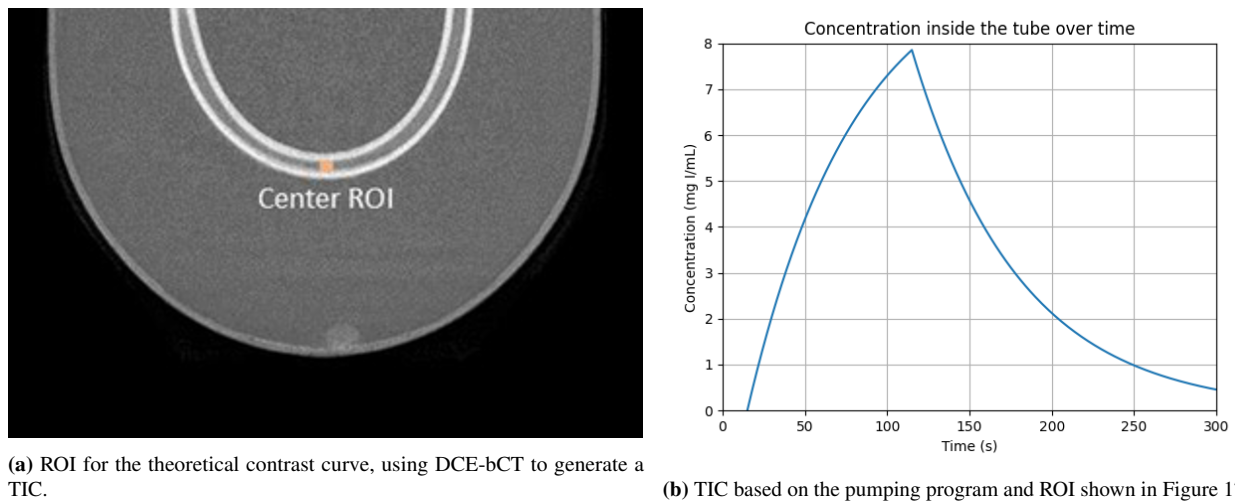
Figure 17: ROI shown on the left, created TIC shown right. Peak contrast concentration is expected around 120 seconds into the measurement [26].

To test the bCT, TICs will be generated for multiple ROIs per phantom design. In addition to individual ROIs for each final phantom design, TICs were created for ROIs inside the inlet and outflow. As supplementary validation for the generated TICs, to represent the conservation of mass within the phantom, these TICs should present similar patterns, with only a time delay between the inlet and outlet.

This chapter presents the final tumor phantom designs and a description of each. An explanation for the chosen ROIs for each, as well as hypotheses for the TICs specific to the design is also presented in this chapter.

5.1   Varying channel phantom

The second measurement session confirmed that the 0.8 mm channel phantom could be filled without trapping air. To introduce different flow patterns within the channel phantom, the diameters of the channels were varied. Given the success of printing and filling 0.8 mm channels air-free in prior designs, we chose to vary the diameters between 0.8 mm and 1.0 mm within a single phantom. Four channels of each diameter were incorporated into the phantom design, as shown in Figure 18.
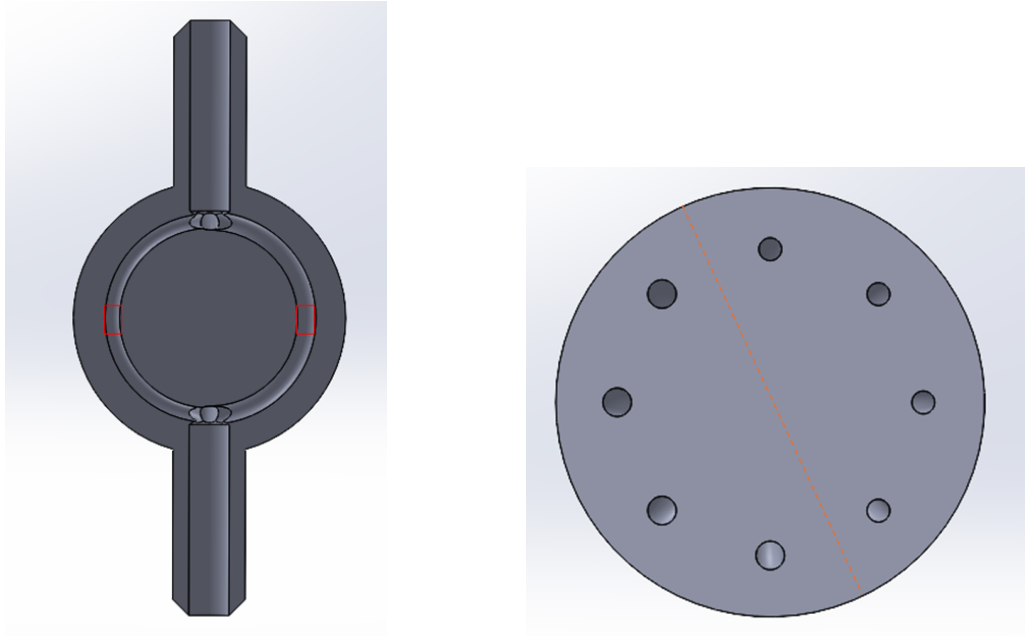
(a) Cross section varying channel phantom. The left channel has a diameter of 0.8 mm, the right channel has a diameter of 1 mm. Red squares indicate regions of interest for TIC analysis.

(b) Front view showing channels with diameters of 0.8 mm and 1 mm. The red dotted line, indicates the split between 1 mm channels on the left side, and 0.8 mm channels on the right.

Figure 18: Different perspectives of the varying channel phantom design.

For the TIC analysis, we expect a sharper increase and decrease in concentration during the wash-in and wash-out phases within the ROI located within the smaller channels. This anticipation is supported by the continuity equation:

$$A_1 \cdot v_1 = A_2 \cdot v_2 \qquad (1)$$

Here, A represents area and v represents velocity. The equations states that the flow on the left must be identical to the flow on the right. For this equation to hold true, the velocity v must be higher in the smaller channels, resulting in a faster wash-in and wash-out of the contrast agent.

5.2 Leaking channel phantom

Another design that leads to different regions within a phantom was also based on the channel phantom. This design is called the leaking channel phantom, referring to the leaking vessels behaviour of tumors. Pores were added onto the channels, which led to a hollow sphere. The hollow sphere is open on the outlet side, making it possible for the fluids to leave the phantom.
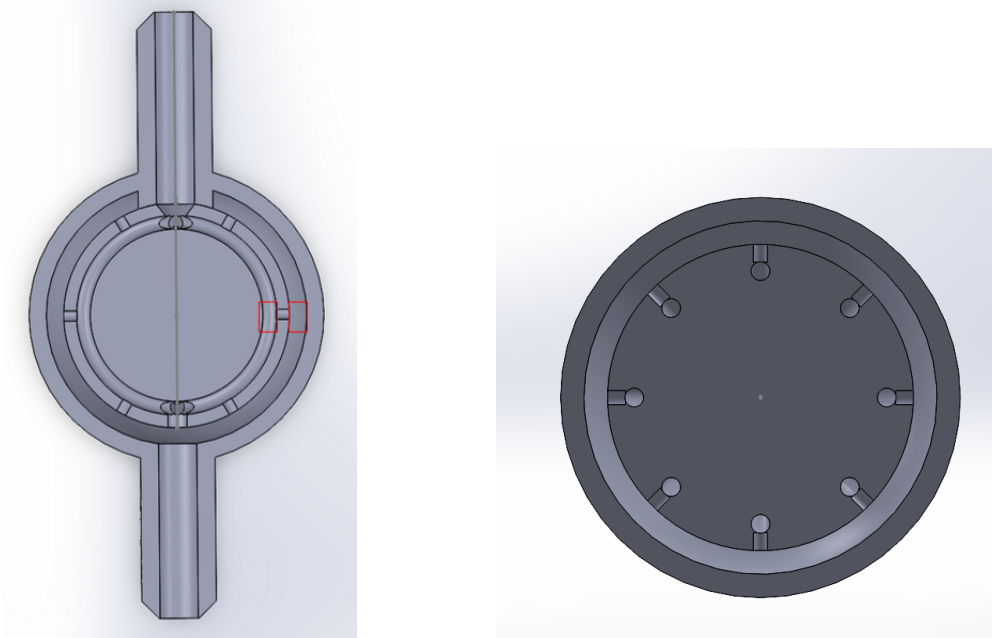
(a) Leaking channel phantom. The phantom has channels with a diameter of 0.8 mm. Three pores are added on top of every channel; the radius of the pores is 0.3 mm. The pores lead to a hollow space inside the phantom.

(b) Leaking channel phantom, sphere cut through the middle. 8 channels with a diameter of 0.8 mm. The hollow space for the leaked mixture is also visible.

Figure 19: Leaking channel phantom images showing different perspectives.

For this design, the inner sphere was created the same as for channel phantoms. This sphere had a radius of 6.5 mm. Three pores with a radius of 0.3 mm were added on top of each channel. These pores led to a hollow space created around the inner sphere. A solid outer sphere with thickness of 1 mm was designed around the hollow cavity. The TICs of a ROI inside hollow sphere as well a an ROI inside the channels were compared with each other.

The TIC for the ROI inside the channels is expected to exhibit a steeper wash-in and wash-out. This is because the channels are directly connected to the inlet and outlet, allowing for rapid changes in contrast concentration. Conversely, in the hollow space, there is a delay before the maximum concentration of contrast is reached, as the contrast first needs to leak into this area. Similarly, the wash-out phase is also prolonged in the hollow space due to this delay.

5.3 Varying gyroid structure

For the varying gyroid phantom design, it was decided to split the phantoms into two halves. This way two different sizes of gyroid structures could be combined into one phantom design. This was done with SOLIDWORKS assembly and two halve gyroid phantoms with different pore sizes. The difference in pore size creates two different flow patterns in each halve, the sizes used were 1.3 mm and 1.5 mm. The form of the phantom was the same as for the 0.8 mm channel phantom. The larger sphere used for the second CB-CT session was not continued for this gyroid phantom, since the first SLA gyroid phantom design with 1.3 mm pores was also successfully filled air-free with the adjusted measurement protocol.
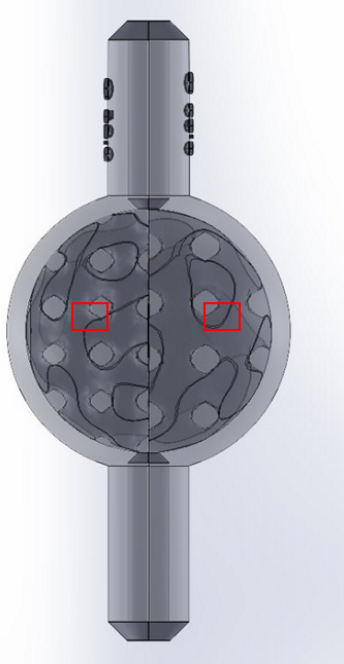
(a) Varying gyroid phantom. The top has a bigger gyroid structure than the bottom, creating two regions within the phantom. ROI is indicated with red squares; TICs are created for these regions.
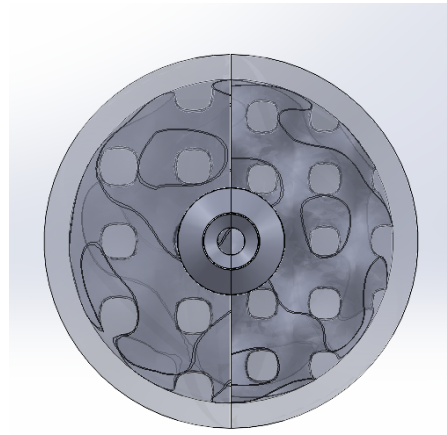
(b) Varying gyroid phantom. The left side has smaller gyroid pores than the right side of the phantom, with 1.3 mm and 1.5 mm pores respectively, leading to two different flow regions inside the phantom.

Figure 20: Different views of the varying gyroid phantom design. Two regions are created, using different sizes of the gyroid pattern.

In the varying gyroid phantom, a quicker wash-in and wash-out are anticipated within the ROI inside the halve with larger pores. This expectation arises from reduced flow resistance in those areas, facilitating an earlier contrast agent peak upon introduction. This phenomenon also accelerates the clearance of the contrast agent when the blood-mimicking fluid begins to enter the phantom.

6   DCE-bCT measurements methode

To validate the different flow patterns within the phantom. DCE-bCT measurements were acquired with the Koning Breast CT at Radboud University Hospital in Nijmegen. The final three phantom designs were chosen for the dynamic measurements: the varying channel design, the leaking channel design and as last the varying gyroid phantom, presented in Chapter 5. The protocol for the dynamic measurements is presented in this chapter.

6.1   Preparations Enschede

Two mixtures were prepared, a blood-mimicking fluid to simulate blood viscosity and a contrast solution with the concentration of 10 mg I/mL . These two mixtures were prepared to create contrast wash-in and wash-out inside the phantoms

1. **Blood-mimicking fluid:**

   - 2L Glycerol
   - 2L Room temperature tap water
   - 40 mL ILFORD ILFOTOL

2. **Contrast Solution:**

   - 325 mL Glycerol
   - 325 mL Room temperature tap water
   - Pink food coloring drops
   - 5 mL Iodine contrast agent

6.2   DCE-bCT preparation protocol

The finalized method to get the phantoms air-free was used, presented in Chatper 4.3.3, before placing the phantom inside the breast phantom. A pump was connected to a container filled with the first mixture. The pump was then connected with a tube to the phantom, and a locking mechanism was used between this connection. On the other side of the phantom, a tube was placed, also with a locking mechanism, the other side of the mechanism was connected with a tube, returning the mixture to the container. This way, the mixture was flushed through the phantom. By ticking against the phantom with fingers and using the mixing plate, all air was removed from the inside of the phantom. Both tubes connected to the phantom were locked using the two t-split parts, enabling air-free pre-filling of the phantom and placement inside the breast phantom. The setup for this air-free filling is presented in Figure 21.
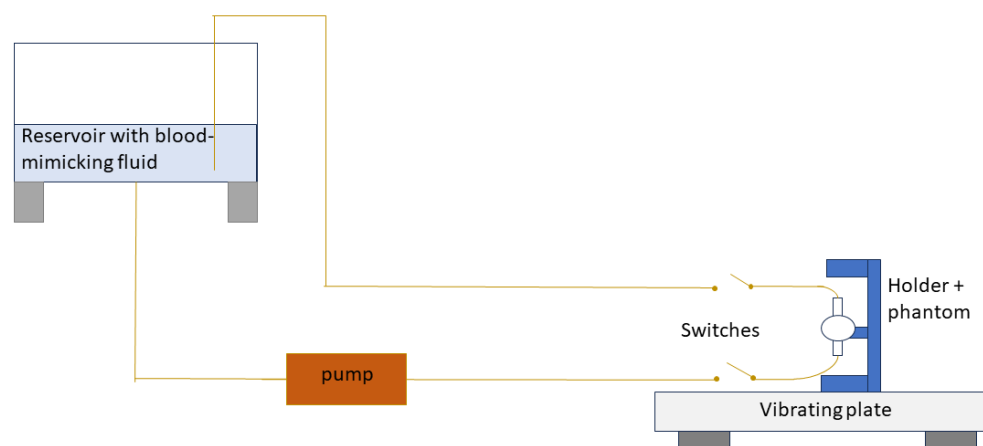
Figure 21: Schematic setup for air-free pre-filling of the phantom. The switches in the diagram represent T-split components used in the setup. These components can block flow in one direction, these components block the flow the phantom is filled. The phantom is than incorporated into the DCE-bCT setup and unlocked.

After the phantom was placed in the breast phantom, the inlet side of the setup was pre-filled with the blood-mimicking fluid. This side was then connected to the phantom, and a small amount of mixture was tapped from this connection point, to prevent air in between the connection point of the phantom and the inlet side of the phantom. The outlet side of the setup side was then also pre-filled with the same mixture and connected to the other side of the phantom.

To create the wash-in and wash-out inside the phantoms, three syringes were prepared. At the inlet side, one of the syringes was prepared with 60 ml of the contrast solution, the other two were filled with blood-mimicking fluid prepared earlier. A syringe pump with two empty syringes was placed on the outlet side, to enforce the flow through the phantom. The setup used for the optical spectrometer data is shown in Figure 22; the setup was placed on top of the bCT.
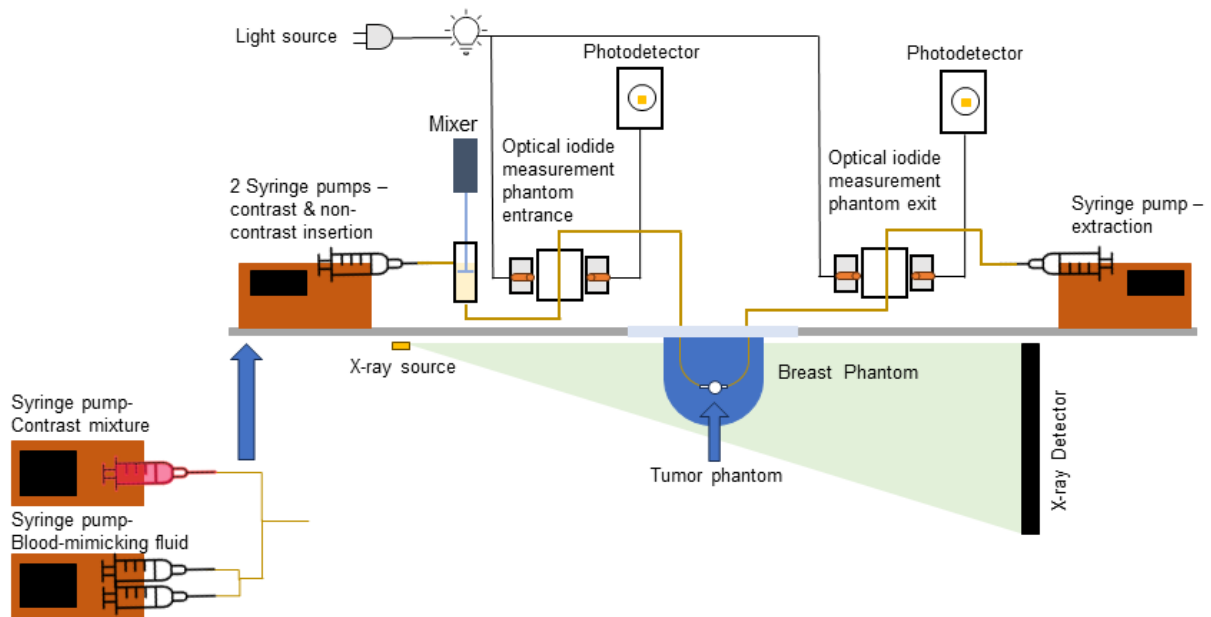
Figure 22: Schematic representation of the optical spectroscopy setup used in Nijmegen on top of the bCT. This setup is used to validate the TICs created with the DCE-bCT [26]. The phantom is added to the setup, as well as additional representation of the inlet pump.

When the setup was prepared, a scout image was created and assessed to be sure that no air was present inside the phantom. This image reconstruct to a low-resolution, single projection image, similar to a plain X-ray. It is used as preparation for detailed cross-sectional scans, ensuring that the scanned area is correctly aligned with the patients ROI. Thereafter, the dynamic scan could be started. The CT scan was started with a special sequence, at the same time as the syringepump programmes started. For the wash-in phase, the outlet syringes were started to extract the fluid, while at the same time, the setup was flushed with blood-mimicking fluid. Before the mixture entered the phantom, a mixer made sure that it was mixed with the blood-mimicking fluid. This way a continuous wash-in was created. After the syringe pump with contrast was done, the pump with blood-mimicking started. This indicated the start of the wash-out phase. The blood-mimicking fluid was mixed with the residue of the contrast mixture before entering the phantom with the residue of mixture two in the setup.

On both sides of the phantom, a spectrometer was placed. Since the blood-mimicking fluid was clear and the contrast mixture had red food colouring added, a optical intensity profile could be created. No contrast concentration statements can be made since the setup was not calibrated, but the wash-in and wash-out profile can be seen. The time of maximum contrast inside the phantom can be estimated with the help of the optical intensity plotted against time, and can be compared to the TIC results, to validate to TICs.

6.3   DCE-bCT sequence

For the DCE-bCT a special sequence is used. This sequence can be seen in Figure 23 and starts after the scout image is assessed. Before the dynamic scan can start the right breast must be selected in the top right red block. The first sequence block of 10 seconds, and creates 360 pulses per revolution. This makes a high spatial resolution reconstruction possible for the breast and tumor phantom. After this block the CT sequence continued with a 20, 125 and 230 seconds block. For this sequence parts, only 40 pulses per revolution are used. Using the high spatial resolution data from the first block, a TIC with high temporal resolution can be generated from this part of the CT scan. With this dynamic scan sequence, a reconstruction can be made with a voxel size of 0.1 mm. The CT sequence was started at the same time as the pumping program.
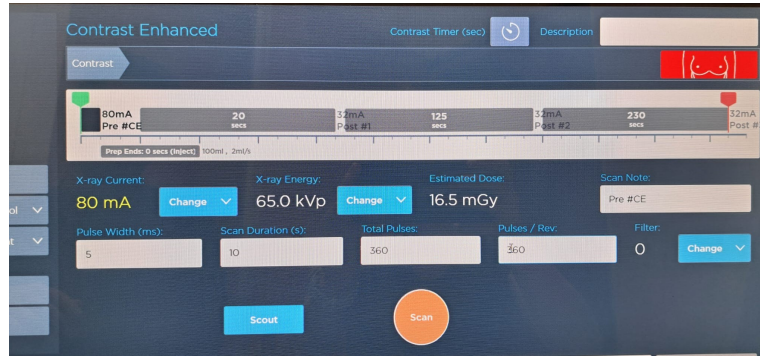
(a) Picture of the starting block for the DCE-bCT measuring sequence.

(b) Picture of the other block for the DCE-bCT measuring sequence.

Figure 23: Figure a and b show the CT sequence used for the DCE-bCT measurement.

7   Results

The optical spectrometer data is presented in this chapter. Due to uncontrollable circumstances, no time intensity curves are presented in this chapter.

7.1   Spectrometer results

The optical intensity is plotted against time for both spectrometers. This measurement can determine the time at which the maximum contrast concentration is present in the phantom. The setup was first filled with blood-mimicking fluid. At the start of the CT measurement, one of the syringe pumps started pumping the contrast mixture for 100 seconds at 24 mL/min. This mixture had food colouring added to it, resulting in a different optical intensity measured by the spectrometer, compared to the clear blood-mimicking fluid. The other syringe pump on the inlet side started to pump blood-mimicking fluid into the setup at 24 mL/min. The optical intensity was expected to be restored to the initial value, indicating all of the contrast mixture left the system. The intensity plots over time should look the same for the spectrometers, with only a time shift expected for the spectrometer at the outlet compared to the inlet spectrometer. A schematic representation of the pumping program is given in Figure 24.

Contrast mixture: 24 mL/min for 100 seconds	Blood-mimicking fluid: 24 mL/min for 200 seconds

Extruding syringes : 24 mL/min for 300 seconds

Figure 24: Schematic representation of pumping program. Creating a wash-in and wash-out phase

Measurement 1: Varying Channel Phantom
The outlet spectrometer shows a clear decrease in optical intensity in the first 200 seconds, indicating that the contrast mixture entered the system. After 200 seconds, the measured intensity increased, and after 350 seconds, the value was restored to the initial value, meaning that all of contrast mixutre had left the system. The data for the inlet and outlet spectrometer is shown in Figure 25a. The inlet spectrometer was expected to show the same behavior ahead of the outlet spectrometer. However, this was not the case, as the inlet spectrometer was not functioning due to misalignment or damage to the optical fibers. Therefore, the decision was made to only look at the outlet spectrometer data. The peak concentration for Experiment 1 is around 200 seconds, marking the turning point from wash-in to wash-out. Figure 25b shows only the optical outlet spectrometer data and the turning point is indicated with a red arrow.
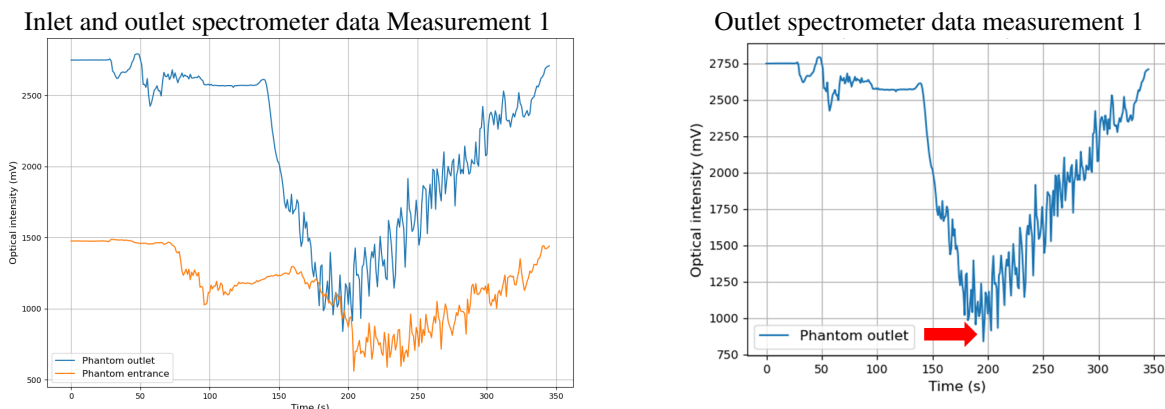
(a) Optical spectrometer data for measurement 1. Varying channel phantom is used in this measurement.

(b) Outlet spectrometer data for measurement 1. Varying channel phantom measured.

Figure 25: Optical spectrometer data for varying channel phantom.

Measurements 2 and 3: Leaking channel phantom and varying gyroid phantom

The data for the optical outlet spectrometer was also plotted against time for these measurements. For Measurement 2, the minimum intensity value is around 180 seconds, and for Measurement 3, it is around 190 seconds. The data for these optical measurements are shown in Figure 26, the time of maximum contrast measured by the outlet spectrometer is indicated with red arrows in the subfigures.
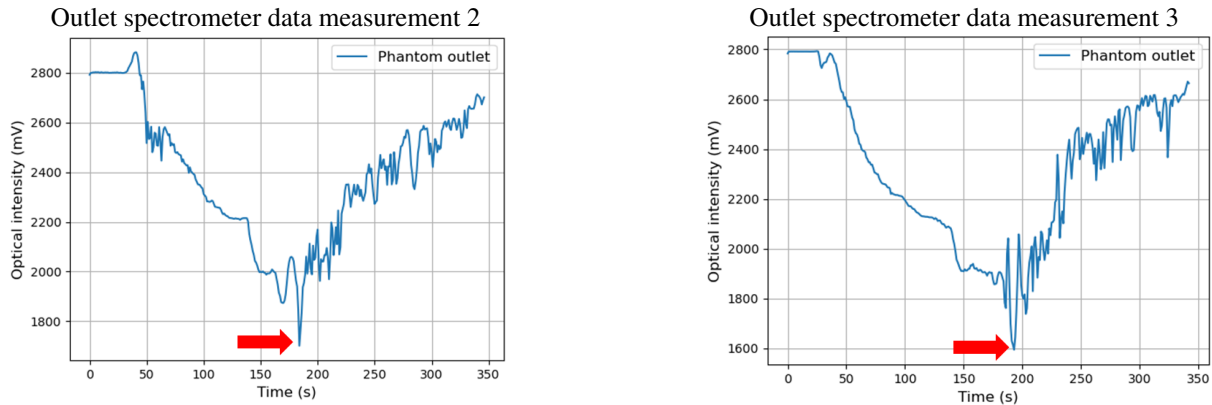
(a) Outlet optical spectrometer data for leaking channel phantom. The highest contrast concentration inside the phantom is reached around 180 seconds.

(b) Outlet optical spectrometer data for varying gyroid phantom. The highest contrast concentration inside the phantom is reached around 190 seconds.

Figure 26: Optical spectrometer data for two different tumor phantoms.

7.2   Time-Intensity Curves

Uncontrollable events have prevented generating of the temporal intensity curves for each of the final designs.

8   Discussion

This study aimed to design a tumor phantom to test DCE-bCT as a possible monitoring technique for breast cancer.

For the phantom designs, a simplified model was used to represent a breast tumor. The size and form of tumors vary significantly among patients, as well as hormone expression, HER-2 status, proliferation index and gene expression. Further research is needed to investigate the influence of these parameters on the usability of DCE-bCT as a monitoring technique. Using patient tumor segmentation as the basis for the form and size of the phantom can be a future step. A start of tumor segmentation is presented in Appendix C.

The small channels, gyroid structures and leaking vessels inside the phantom represent the internal vascular structure of the tumors. However, this is a simplified representation of the vascular structure inside a real tumor. For future testing, more complex vascular structures must be designed within a phantom. This allows to test distinguishability between the heterogeneous regions inside the phantom more comprehensive.

The final designs were produced using an SLA printer. This production technique has some noteworthy discussion points. The resolution of the printer in the x and y directions determines how accurately the sketch is followed and if the sizes of the prints match those of the design sketches. The z-resolution determines the accuracy of the layer thickness and thus influences the accuracy in the representation of the sketch in the print. Regular calibration of the printer reduces the influence of this factor. Cleaning the prints rigorously is essential to ensure all the excess resin is removed. If not done correctly, the sizes of the channels and gyroid pores can differ within the phantom, affecting the flow inside the ROIs. The phantoms with channels are symmetrical, making it possible to compare multiple matching ROIs. Averaging the findings of the ROIs minimizes the possible differences per ROI. With the help of air, syringes and IPA bath, the prints are now cleaned. Testing a more reliable cleaning method would enhance the results for all three final designs, allowing for interchangeability between two prints of the same phantom and obtaining consistent results. Currently, the individual prints of the same design show too much difference for that to be possible.

The first step of the DCE-bCT measurements is filling the phantoms air-free. A static scan assessed that no air was present inside the phantom. However, microbubbles might have been introduced in the phantom setup after this step. These bubbles could influence the findings inside the ROI since the attenuation coefficient of air is smaller than that of both fluid mixtures used. For a better assessment, the attenuation coefficient for each voxel can be determined for the scout image. This strengthens the assessment of the phantom being filled air-free.

The mixer in the setup creates a constant wash-in and wash-out inside the phantom. When the blood-mimicking fluid and contrast are not thoroughly mixed, this can lead to an inconsistent contrast profile. This will be reflected in the TICs created for the different ROIs inside the phantoms. With the spectrometer calibrated and both working, a better estimation can be made for the contrast concentration over time; this is useful information to validate the results gathered in the TICs. For this research, the time of maximum contrast inside the phantom is based on the optical outlet spectrometer. Before the maximal contrast concentration reaches the outlet spectrometer, it passes through the phantom. Making an estimated guess for maximal contrast concentration inside the phantom is possible; however, a more reliable method to determine this time is worth investigating.

The ROIs on the scans are manually selected using design sketches, which show the essential sizes of the phantom to select the ROIs. However, the regions may not be selected correctly and may contain material of the tumor phantom. Since the phantom is solid, no flow is possible in these regions, affecting the TIC for the selected regions. Averaging over comparable ROI inside a phantom can overcome part of this problem.

The outlet spectrometer data showed the expected flow pattern for the contrast through the phantoms. Inlet data would have been beneficial for determining the specific time for maximum contrast inside the phantom. This contrast peak was achieved, exactly between the inlet and outlet measured peak.

So far, no other 3D-printed X-ray breast tumor phantoms have been presented in the literature. Earlier studies showed moulding technique or used small tubes for a tumor phantom design. The study by Ng. et al presented an FDM 3D printed modular liver tumor phantom created with a micron gyroid structure (pore size: 500 to 2000 μm). In this study, SLA printed modular phantoms were created with the advantage of higher durability, precision and water tightness. Furthermore, three varying designs with small channels (0.8 mm), leaking regions, small gyroid structures and heterogeneous perfusion regions have been presented. The phantoms were originally designed for optimizing DCE-bCT but can also be used in other X-ray imaging techniques such as conventional CT, mammography, and DBT. Furthermore, they were developed to mimic breast tumors specifically, but their shape and size can be easily adapted to mimic other types of cancer.

9   Conclusion

This research presented three final tumor phantom designs that are compliant with the setup. The final designs fulfill the requirements set at the start. The outlet optical spectrometer showed a successfully created wash-in and wash-out. Due to unforeseen circumstances, no Time-Intensity Curves have been created to further test Dynamic Contrast-Enhanced Breast Computed Tomography as monitoring technique.

References

[1] Who WHO. Breast cancer. World Health Organization: WHO. 2024 Mar. Available from: `https://www.who.int/news-room/fact-sheets/detail/breast-cancer`.

[2] Sung H, Ferlay J, Siegel RL, Laversanne M, Soerjomataram I, Jemal A, et al. Global Cancer Statistics 2020: GLOBOCAN Estimates of Incidence and Mortality Worldwide for 36 Cancers in 185 Countries. CA Cancer J Clin. 2021 May;71(3):209-49. doi:10.3322/caac.21660.

[3] DeSantis CE, Ma J, Gaudet MM, Newman LA, Miller KD, Sauer AG, et al. Breast cancer statistics, 2019. CA Cancer J Clin. 2019 Nov;69(6):438-51. doi:10.3322/caac.21583.

[4] Mammography; 2024. [Online; accessed 25. Apr. 2024]. Available from: `https://www.nibib.nih.gov/science-education/science-topics/mammography`.

[5] Lei S, Zheng R, Zhang S, Wang S, Chen R, Sun K, et al. Global patterns of breast cancer incidence and mortality: A population-based cancer registry data analysis from 2000 to 2020. Cancer Commun. 2021 Nov;41(11):1183. doi:10.1002/cac2.12207.

[6] Bevolkingsonderzoek borstkanker | RIVM; 2024. [Online; accessed 17. Apr. 2024]. Available from: `https://www.rivm.nl/bevolkingsonderzoek-borstkanker`.

[7] ; 2023. [Online; accessed 25. Apr. 2024]. Available from: `https://www.rivm.nl/sites/default/files/2023-12/Monitor-2022-breast-cancer.pdf`.

[8] Grimm LJ, Avery CS, Hendrick E, Baker JA. Benefits and Risks of Mammography Screening in Women Ages 40 to 49 Years. Journal of Primary Care & Community Health. 2022 Jan;13. doi:10.1177/21501327211058322.

[9] Dense Breasts: Answers to Commonly Asked Questions; 2024. [Online; accessed 25. Apr. 2024]. Available from: `https://www.cancer.gov/types/breast/breast-changes/dense-breasts`.

[10] ; 2023. [Online; accessed 18. Jun. 2024]. Available from: `https://marketing.webassets.siemens-healthineers.com/0d5f6b4096e3c42c/6df660c567fb/siemens_healthineers_xp_3d-mammogram-technology_malmoe_-screening_trial.pdf`.

[11] Bernardi D, Ciatto S, Pellegrini M, Tuttobene P, Fanto' C, Valentini M, et al. Prospective study of breast tomosynthesis as a triage to assessment in screening. Breast Cancer Res Treat. 2012 May;133(1):267-71. doi:10.1007/s10549-012-1959-y.

[12] Sprague BL, Coley RY, Lowry KP, Kerlikowske K, Henderson LM, Su YR, et al. Digital Breast Tomosynthesis versus Digital Mammography Screening Performance on Successive Screening Rounds from the Breast Cancer Surveillance Consortium. Radiology. 2023 May. Available from: `https://pubs.rsna.org/doi/10.1148/radiol.223142`.

[13] Ali RMKM, England A, Tootell AK, Hogg P. Radiation dose from digital breast tomosynthesis screening - A comparison with full field digital mammography. J Med Imaging Radiat Sci. 2020 Dec;51(4):599-603. doi:10.1016/j.jmir.2020.08.018.

[14] Durand MA. Synthesized Mammography: Clinical Evidence, Appearance, and Implementation. Diagnostics. 2018 Jun;8(2). doi:10.3390/diagnostics8020022.

[15] Niell BL, Freer PE, Weinfurtner RJ, Arleo EK, Drukteinis JS. Screening for Breast Cancer. Radiol Clin North Am. 2017 Nov;55(6):1145-62. doi:10.1016/j.rcl.2017.06.004.

[16] Smith DN. Breast ultrasound. Radiol Clin North Am. 2001 May;39(3):485-97. doi:10.1016/s0033-8389(05)70293-1.

[17] Berg WA, Zhang Z, Lehrer D, Jong RA, Pisano ED, Barr RG, et al. Detection of breast cancer with addition of annual screening ultrasound or a single screening MRI to mammography in women with elevated breast cancer risk. JAMA. 2012 Apr;307(13):1394-404. doi:10.1001/jama.2012.388.

[18] Lau D, Corrie PG, Gallagher FA. MRI techniques for immunotherapy monitoring. J ImmunoTher Cancer. 2022;10(9). doi:10.1136/jitc-2022-004708.

[19] Meaney C, Rhebergen S, Kohandel M. In silico analysis of hypoxia activated prodrugs in combination with anti angiogenic therapy through nanocell delivery. PLoS Comput Biol. 2020 May;16(5). doi:10.1371/journal.pcbi.1007926.

[20] Dvorak HF. Leaky tumor vessels: consequences for tumor stroma generation and for solid tumor therapy. Prog Clin Biol Res. 1990;354A:317-30.(;):Prog. Available from: `https://pubmed.ncbi.nlm.nih.gov/2247496`.

[21] Mo T, Brandal SHB, Geier OM, Engebråten O, Nilsen LB, Kristensen VN, et al. MRI Assessment of Changes in Tumor Vascularization during Neoadjuvant Anti-Angiogenic Treatment in Locally Advanced Breast Cancer Patients. Cancers. 2023 Sep;15(18). doi:10.3390/cancers15184662.

[22] Linh LT, Duc NM, My TTT, Bang LV, Thong PM. Correlations between dynamic contrast-enhanced magnetic resonance imaging parameters and histopathologic factors in breast cancer. Clin Ter. 2021 Sep;172(5):453-60. doi:10.7417/CT.2021.2358.

[23] Li X, Arlinghaus LR, Ayers GD, Chakravarthy AB, Abramson RG, Abramson VG, et al.

[24] Caballo M, Mann R, Sechopoulos I. Patient-based 4D digital breast phantom for perfusion contrast-enhanced breast CT imaging. Med Phys. 2018 Oct;45(10):4448-60. doi:10.1002/mp.13156.

[25] Goris L, Mikerov M, Manohar S, Sechopoulos I. In-line spectroscopy for the quantification of iodine in a breast perfusion phantom for dynamic contrast-enhanced dedicated breast CT imaging validation. In: Proceedings Volume 12925, Medical Imaging 2024: Physics of Medical Imaging. vol. 12925. SPIE; 2024. p. 795-9. doi:10.1117/12.3006763.

[26] Goris L, Pautasso J, Mikerov M, Michielsen K, Sechopoulos I. Perfusion phantom for the optimization of dynamic contrast-enhanced dedicated breast CT: iodine contrast curves in a simplified breast phantom. In: Proceedings Volume 13174, 17th International Workshop on Breast Imaging (IWBI 2024). vol. 13174. SPIE; 2024. p. 195-200. doi:10.1117/12.3026996.

[27] Meaney C, Rhebergen S, Kohandel M. In silico analysis of hypoxia activated prodrugs in combination with anti angiogenic therapy through nanocell delivery. PLoS Comput Biol. 2020 May;16(5):e1007926. doi:10.1371/journal.pcbi.1007926.

[28] Koning Vera Breast CT System, US; 2024. [Online; accessed 12. Jun. 2024]. Available from: `https://www.medicaldevice-network.com/projects/koning-vera-breast-ct-system-us`.

[29] Stages of Breast Cancer | Understand Breast Cancer Staging; 2024. [Online; accessed 21. Jun. 2024]. Available from: `https://www.cancer.org/cancer/types/breast-cancer/understanding-a-breast-cancer-diagnosis/stages-of-breast-cancer.html`.

[30] Cserni G, Chmielik E, Cserni B, Tot T. The new TNM-based staging of breast cancer. Virchows Arch. 2018 May;472(5):697-703. doi:10.1007/s00428-018-2301-9.

[31] Grand-Perret V, Jacquet JR, Leguerney I, Benatsou B, Grégoire JM, Willoquet G, et al. A Novel Microflow Phantom Dedicated to Ultrasound Microvascular Measurements. Ultrason Imaging. 2018 Jun;40(5):325-38. doi:10.1177/0161734618783975.

[32] Lin J, Hsiung K, Ritenour R, Golzarian J. 3D reconstruction of microvascular flow phantoms with hybrid imaging modalities. In: Medical Imaging 2011: Visualization, Image-Guided Procedures, and Modeling; 2011. p. 79642H. doi:10.1117/12.878205.

[33] Ng D, Nikolov HN, Tai E, Gelman D, Drangova M. Modular 3D-printed liver tumour phantom for modelling embolization procedures. ResearchGate. 2024 Mar:48. doi:10.1117/12.3004837.

[34] 3D printing with Gyroid Infills: all you need to know! – 3D Solved; 2024. [Online; accessed 20. Jun. 2024]. Available from: `https://3dsolved.com/3d-printing-with-gyroid-infills-all-you-need-to-know`.

[35] FDM vs. SLA: Compare Filament and Resin 3D Printers; 2024. Formlabs, [Online; accessed 12. Jun. 2024]. Available from: `https://formlabs.com/eu/blog/fdm-vs-sla-compare-types-of-3d-printers`.

[36] FDM 3D Printing: How it Works; 2024. [Online; accessed 20. Jun. 2024]. Available from: `https://www.crossproductdesign.com/fdm-3d-printing-how-it-works`.

[37] Hansen J. SLA 3D Printer Guide. Parts Badger. 2022 Apr. Available from: `https://parts-badger.com/sla-3d-printer-guide`.

[38] Mettivier G, Sarno A, Varallo A, Russo P. Attenuation coefficient in the energy range 14-36 keV of 3D printing materials for physical breast phantoms. Phys Med Biol. 2022 Sep;67(17):. doi:10.1088/1361-6560/ac8966.

[39] Saito M. Dual-energy approach to contrast-enhanced mammography using the balanced filter method: spectral optimization and preliminary phantom measurement. Med Phys. 2007 Nov;34(11):4236-46. doi:10.1118/1.2790841.

[40] A11. How to Create a Gyroid Surface in SolidWorks. Youtube; 2023. [Online; accessed 22. Jun. 2024]. Available from: `https://www.youtube.com/watch?v=PJovx-ytJYI`.

[41] Cheng NS. Formula for the Viscosity of a Glycerol-Water Mixture. Ind Eng Chem Res. 2008 May;47(9):3285-8. doi:10.1021/ie071349z.

Appendix A: Leaking gyroid phantom

A counterpart for the leaking channel phantom was also designed. The gyroid phantom was combined with leaking aspect of the leaking channel phantom. For this design the gyroid structure with 1.5 mm pores was used. Twenty-four pores were created inside this phantom. The pores lead to an outer hollow shell. The hollow sphere had no opening toward the outlet. Making this phantom unsuitable for testing, since the contrast mixture was not able to leave the cavity. For the leaking channel phantom, this was alterd, making it suitable for DCE-bCT testing. Depending on the results, this alteration could be interesting for this design as well. The Leaking gyroid phantom can be seen in Figure 27.
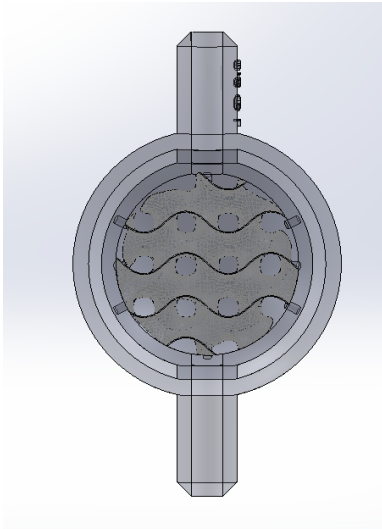
(a) Cross section of the leakin gyroid phantom. Gyroid pores have a diameter of 1.5 mm. Leaking pores have a diameter of 0.6 mm.
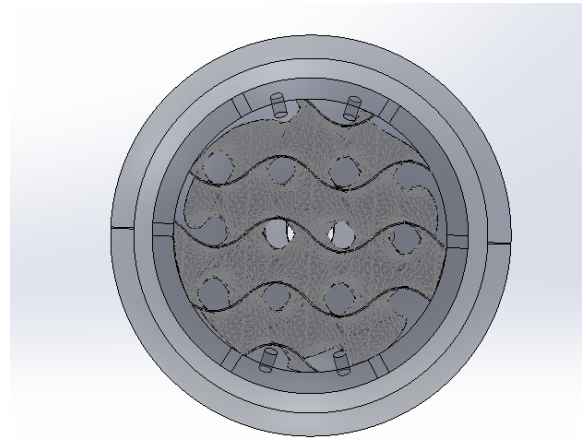
(b) Front view of the leaking gyroid phantom. Hollow cavity is visible, as well as the gyroid structure and leakage pores.

Figure 27: Overview of the leaking gyroid phantom design.

Appendix B: Overview of the designed phantoms

FDM Gyroid phantom

Not able to test, the phantom is not waterproof, and no flow is possible through the phantom, since inlet and outlet are clogged wit PLA.

SLA printed phantoms
Channel phantom

Diameter (mm)	Usable
2.2	Yes, CB-CT tested
1.1	Yes, CB-CT tested
0.8	Yes, CB-CT tested
0.5	No (no flow possible)

Dubble channel phantom

Diameter (mm)	Usable
1.1	Yes, CB-CT tested

Gyroid phantom

Pore diameter	Usable
1.1 mm	Yes, CB-CT tested
1.3 mm	Yes, CB-CT tested
1.5 mm	Yes, CB-CT tested
1.5 (18 mm diameter sphere)	Yes, CB-CT tested

Varying channel phantom <-- Final design

Diameter	**Tested**
0.8 and 1.0 mm	Yes, DCE-bCT tested
0.8, 0.9, 1.0 and 1.1 mm channels (phantom channels are split in four, each 2 channels)	Not tested due to time

Leaking channel phantom <-- Final design

Diameter (channels/pore)	**Tested**
0.8 / 0.6 mm	Yes, DCE-bCT tested
0.8 / 0.4	Not tested due to time
0.8, 0.9, 1.0 and 1.1 mm channels (phantom channels are split in four, each 2 channels)/ 0.6 mm	Not tested due to time

Varying gyroid phantom <-- Final design

| Pore sizes (halve/halve)	Usable
1.3 / 1.5 mm	Yes, CB-CT tested
1.1 / 1.5 mm	Not tested due to time
1.1 / 1.3 mm	Not tested due to time

Leaking gyroid phantom

Pore sizes (Gyroid/leaking pores)	Usable
1.5 / 0.6 mm	Not suitable

Appendix C: Tumor Segmentation

This research made a first attempt at tumor segmentation. Four CT scans from patients with breast cancer treated at Radboud Hospital in Nijmegen were provided. The scale of the CT scans was not provided, making it impossible to say something about the difference in size between the tumors. However, the diversity in tumour form can be seen.

Table 2: Tumor segmentation from for patients bases on CT images

Tumour segmentation from CT scans for four random patients.
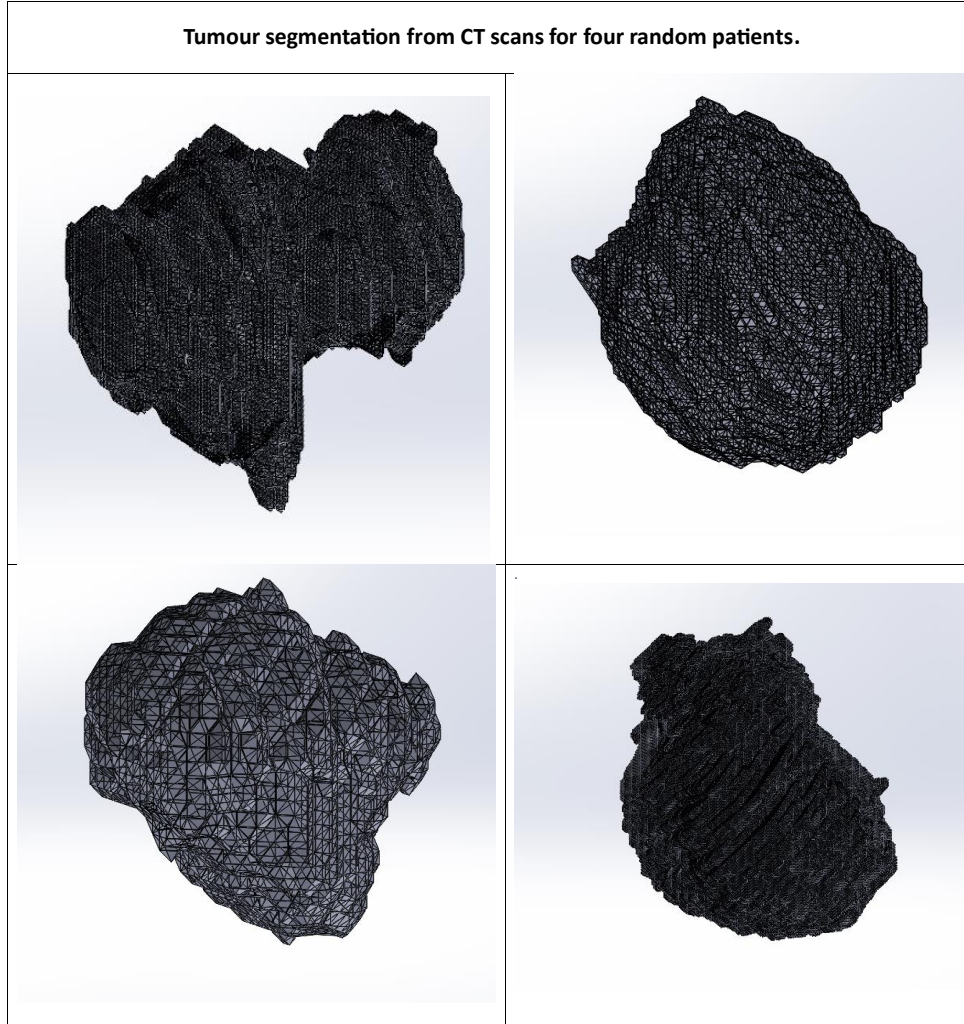
The code used to segment the tumors from the CT scan is provides below.

```python
# First import the following using this command in your
terminal: pip install tifffile scikit-image trimesh
import tifffile as tiff
from skimage import measure
import trimesh


# Load the TIF image
tiff_image = tiff.imread('test4.tif')


# Ensure the image is a 3D array
if tiff_image.ndim != 3:
raise ValueError("The loaded TIFF image is not 3D.")


# Apply marching cubes algorithm to extract the mesh
# `level` is the threshold value to consider for the isosurface.
To create finer meshes you can make this number smaller.
vertices, faces, normals, values =
measure.marching_cubes(tiff_image, level=0.1)


# Create a Trimesh object
mesh = trimesh.Trimesh(vertices=vertices, faces=faces,
vertex_normals=normals)


# Export the mesh to an STL file
mesh.export('output_mesh4.1.stl')
```